applied sciences

MDPI

Article

Numerical Simulation of the Hydrodynamic Performance and Self-Propulsion of a UUV near the Seabed

Xiaodong Liu [1], Yuli Hu [1], Zhaoyong Mao [2,*] and Wenlong Tian [1,*]

[1] School of Marine Science and Technology, Northwestern Polytechnical University, Xi'an 710072, China; nwpuliuxiaodong@163.com (X.L.); zx670821@nwpu.edu.cn (Y.H.)
[2] Unmanned Systems Research Institute, Northwestern Polytechnical University, Xi'an 710072, China
* Correspondence: maozhaoyong@nwpu.edu.cn (Z.M.); tianwenlong@nwpu.edu.cn (W.T.)

Abstract: Unmanned underwater vehicles (UUV) face maneuverability and rapidity challenges when they are applied for detecting and repairing submarine oil and gas pipelines, and fiber cables near the seabed. This research establishes numerical models of the bare UUV and self-propelled UUV near the seabed using the computational fluid dynamics (CFD) method. The effect of dimensionless distance Hd and Re_L on the hydrodynamic performance of the vehicle and the interaction between the hull and the propeller is investigated. The range of Hd is 1.5D–10D, and the Re_L is 9.97×10^5~7.98×10^6. Findings indicate that: (1) There is an obvious strong coupling between the hydrodynamic performance of the bare UUV and Hd. With the increase of Hd, the hydrodynamic performance such as C_d, the absolute value of C_l and m_y decreases continuously and finally tends to be stable. The absolute values of C_d and C_l increase with the increase of Re_L. The change trend of m_y is opposite to that of C_l. (2) The variation trend of hydrodynamic performance of the self-propelled UUV with Hd is consistent with those of the bare UUV. Additionally, it increases to some extent, respectively, compared with the bare UUV. (3) The self-propelled characteristics such as t, η_H, w and η_i are weakly related to Hd. The t and η_i increase with the increasing of Re_L, while η_H and w decrease with the increasing of Re_L.

Keywords: hydrodynamic performance; CFD; self-propulsion; seabed; UUV

Citation: Liu, X.; Hu, Y.; Mao, Z.; Tian, W. Numerical Simulation of the Hydrodynamic Performance and Self-Propulsion of a UUV near the Seabed. *Appl. Sci.* **2022**, *12*, 6975. https://doi.org/10.3390/app12146975

Received: 25 May 2022
Accepted: 6 July 2022
Published: 9 July 2022

1. Introduction

UUV is a kind of underwater vehicle, which integrates technologies of underwater communication, automatic control, mode recognition, and artificial intelligence. It is capable of performing underwater tasks autonomously without any operator and is important equipment for exploring the ocean. The UUV has been widely used in marine environment exploration, undersea oil and gas pipeline and cable inspection, hydrological research, etc. The operability and rapidity of UUV are receiving more and more attention, which reflects the safe operations and navigation efficiency of the vehicles. They play an important role in traveling distance and duration of travel. The operability is mainly represented by the hydrodynamic characteristics of the vehicle, and the rapidity generally needs to consider interferences between hull and thruster. In recent years, a great number of studies have studied the hydrodynamic characteristics of UUV and the interaction between hull and thruster through experiments and CFD methods.

The drag and self-propulsion analysis of SUBOFF with E1619 propeller was carried out using CFD method by Sezen et al. [1,2]. The propellers of self-propelled submarines were modeled using the actuated disc and real propellers, respectively. The numerical results are compared with the available experimental data. The suitability of CFD methods for the prediction of self-propulsion performance of underwater vehicles is discussed. Posa et al. [3] reported the results of self-propelled SUBOFF and compared with the towing test results. They find that the bimodal distribution of turbulent stresses in the towing case is different with the axial peak of turbulent kinetic energy in self-propulsion due to the

backpressure gradient induced by the stern section. Carria et al. [4] studied the effect of mesh refinement on propeller performance and wake flow for E1619 propeller and SUBOFF by CFD method. The results showed the applicability of different turbulence models for propeller wake flow and blade tip vortex analysis, and analyzed the self-propulsion performance of SUBOFF.

The near-surface and subsea conditions are two extreme conditions for UUV, which put the maneuverability of UUV to severe challenges. The UUV need to navigate near the surface in order to share, transmit information, obtain energy and update their position. In the near-subsea condition, the UUV detects submarine oil and gas pipelines and fiber optic cables. These two conditions need to consider the nonlinear effect of waves on the vehicles near the surface and the blocking effect of the seabed.

Studies on the interaction between the hull and the propeller near the surface and fully submerged were carried out in a towed tank [5]. The experimental results show that the drag coefficient of UUV in the surface condition is larger than that in the submerged condition. Besides, the reliability of CFD method is verified by the experimental results. It provides a new method to study the interference between hull and propeller. Tian et al. [6] used the two-phase flow calculation CFD method to study the performance of UUV under the wave-current coupling. It's found that the lift of the UUV is greatly influenced by waves, and the average drag increases with the increase of wave height and the decrease of submerged depth. Carria [7] studied the hydrodynamic performance of the SUBOFF with an E1658 propeller near the water surface by experiments and CFD overlapping mesh method. The interaction between the vessel and free surface strongly influences the inflow and wake of the propeller, generating high local propulsion coefficients and blade loads near the propeller surface. Strong surface fluctuations at small axial depths lead to instability and collapse of propeller tip vortices in the near field. The performance of the UUV with a propeller near water surface was simulated by Zhang et al. [8] using the slip grid technique and the VOF method. Results show that the effect of the free surface on the drag force is greater than that of the self-propulsion.

Hydrodynamic characteristics and self-propulsion performance of self-propelled of UUV near the water surface have been carried out by a large number of researchers using CFD and experimental methods. However, there are few papers studying the near-subsea conditions to the authors' knowledge. Song et al. [9–11] proposed two subsea stationing strategies, hydraulically supported and mooring chain types, for UUV that require permanent fixed-point exploration. Two simulation models of the landing process of UUV were established. The results show that the lateral force of UUV with vertical thrust is 5~15% larger than that without vertical thrust. Zhang et al. [12] developed a mathematical model of critical instability considering the complex coupling between the glider and the seabed as well as the flow field in which the underwater glider resides stably. The results show that the center of buoyancy is 0.3 m from the seabed and the angle of attack of the glider has a strong influence on the stability of the system.

However, the UUV analyzed in these papers are stationary without motion. Zhu et al. [13] conducted a model resistance test for UUV at different distances near the seabed and near the sea surface, and established a model test and analysis method to obtain the influence rules of UUV drag near the seabed and near the sea surface. The results demonstrate that considering only the effect of the free surface, it can be assumed that there is no wave resistance when the vessel travels at a depth of over 1/3 of its length. Taking into account only the influence of the seabed wall, the effect of the seabed is no longer considered when the submerged body travels at a distance of over 1/4 of its length from the seabed. When the influences of both free water surface and sea bed wall exist, to completely avoid the interference of restricted water, it is required that submerged hull dive depth exceeds 1/3 of the hull length, and the distance between the seabed and the axis of the submerged hull should not be less than 1/2 of the hull length.

Du et al. [14] developed a numerical model of the near-subsea UUV maneuverability and investigated the effects of distance from subsea, *Re* and angle of attack on the hydrody-

namic performance of the UUV. The results show that the drag coefficient of UUV increases with decreasing distance from the seabed and with increasing angle of attack. The absolute value of the lift coefficient increases with decreasing distance and with the increment of the angle of attack. The absolute value of the pitching moment coefficient increases as the distance decreases and the angle of attack increases. Yan et al. [15] established a numerical model of a near-subsea UUV in order to obtain the effects of subsea boundary effects and complex terrain on the operational stability and maneuverability. The effects of subsea distance, *Re*, angle of attack, and inclined terrain on the hydrodynamic performance of the UUV were analyzed.

In summary, there is little experimental and CFD literature on UUV near the seabed. The studies focus on the hydrodynamic characteristics of UUV, while those of self-propelled UUV are still relatively few. Therefore, it is meaningful to investigate the hydrodynamic performance and self-propulsion performance of the UUV near the seabed through CFD method in this paper. Two models, bare UUV and self-propelled UUV near the seabed, were established and analyzed the effects of *Hd* and Re_L on the performance of vessel.

2. Studied Configuration

2.1. UUV Geometry Parameters

The self-propelled UUV used in this research includes three parts: the main body of the vessel (hull), the fin plates and the propellers, as shown in Figure 1. The hull profile is generated using the theoretical equation proposed in reference [6]. Its total length is 2 m and the maximum diameter is 0.2 m. It can be divided into three parts: nose, parallel section and tail end, with the lengths of 0.3 m, 1.2 m and 0.5 m, respectively. The main parameters of the UUV hull are shown in Table 1. To match the hull, a scaled-down 0.6× DTMB4119 model propeller is used for the propulsion section, with a diameter of 0.1829 m. Detailed parameters are shown in Table 2. The hub of the propeller is suitably altered to match the stern of the hull.

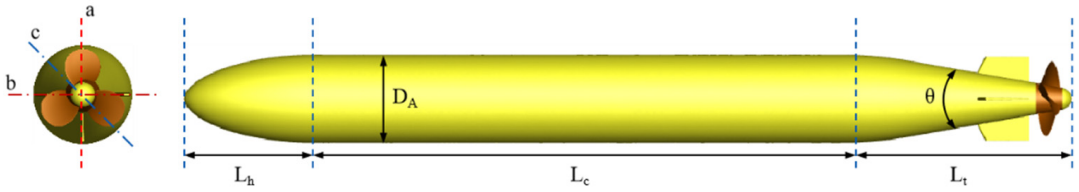

Figure 1. (**a**) Lateral view of self-propelled UUV; (**b**) front view of self-propelled UUV.

Table 1. Main parameters of UUV hull.

Parameter	Value	Parameter	Value
D_A	0.2 m	L_t	0.5 m
L_A	2 m	θ	20°
L_h	0.3 m	U	Variable
L_c	1.2 m	Hd	Variable

Table 2. Detailed parameters of the propeller DTMB4119.

DTMB 4119 Model Propeller	
D (m)	0.1829
Z	3
Skew (°)	0
Rake (°)	0
Blade section	NACA66 a = 0.8
Rotation direction	Right
Scaling	0.6

2.2. Definition of Dimensionless Parameters

In order to classify the computational cases and analyze the effects of Hd and Re_L on the rapidity and maneuverability of the UUV more conveniently, the dimensionless parameter Hd, which is the ratio of the distance between the seabed and the axis of UUV to the maximum diameter of the UUV, is introduced in this paper. Additionally, the values of Hd are 1.5, 2, 2.5, 3, 5, 7, 9 and 10, which cover the extreme conditions of subsea exploration in practices. The oncoming velocity takes values in the range of 0.5 m/s, 1 m/s, 2 m/s, and 4 m/s, and the corresponding Re_L ranges from 9.97×10^5 to 7.98×10^6 depending on the length dimension of the vessel. The 3D dimensionless coefficients of drag, lift and pitch moment coefficients are used to describe the hydrodynamic characteristics of the UUV, respectively, which are calculated using following formula.

$$Hd = H/D_{max} \tag{1}$$

$$C_d = \frac{F_x}{\frac{1}{2}\rho S_A U^2} \tag{2}$$

$$C_l = \frac{F_z}{\frac{1}{2}\rho S_A U^2} \tag{3}$$

$$m_y = \frac{M_y}{\frac{1}{2}\rho S_A L_A U^2} \tag{4}$$

C_d, C_l and m_y describe the hydrodynamic characteristics of the UUV. The formulas F_x, F_z and M_y the drag, lift and pitch moment of the UUV. S_A is the maximum cross-sectional area of the UUV. U is the speed of the vehicle. L_A is the total length of the UUV. ρ is the fluid density taken as 998 kg/m^3.

$$J_0 = \frac{V_A}{nD} \tag{5}$$

$$K_T = \frac{T}{\rho n^2 D^4} \tag{6}$$

$$K_Q = \frac{Q}{\rho n^2 D^5} \tag{7}$$

J_0, K_T and K_Q are the propeller open water performance parameters. J_0 is an important parameter for propeller's performance, which is similar to the angle of attack in wing theory. V_A is the velocity at the propeller disc; n is the rotational speed of propeller in rps; D is the propeller diameter. K_T and K_Q are the propeller thrust and torque coefficients, with T and Q being the propeller thrust and torque.

$$t = \frac{R - R_0}{T} \tag{8}$$

$$w = 1 - \frac{J_0}{J} \tag{9}$$

$$\eta_i = \frac{K_{Q_0}}{K_Q} \tag{10}$$

$$\eta_H = \frac{1 - t}{1 - w} \tag{11}$$

The dimensionless parameters t, w, η_i and η_H depict the interaction between the hull and propeller. t describes the effects of the propeller on the drag characteristics of the hull. R is the drag of the self-propelled UUV. R_0 is the drag of the bare UUV at the corresponding speed. Additionally, T is the thrust provided by the propeller on the aft of the UUV. In the absence of scaling effects, R and T are equal. w and η_i define the effects of the wake field of the self-propelled UUV on the propeller performance. J and K_Q are the feed ratios and

torque coefficients of the propeller of the self-propelled UUV. J_Q and K_{Q_0} are the feed ratios and torque coefficients of the propeller in open water condition derived by using the equal thrust method. η_H describes the hull efficiency and represents the combined effect of thrust reduction and wake fraction.

The calculation cases in this paper are classified into two main categories, as shown in Table 3.

Table 3. Simulation case classification.

Group	Description	*Hd*	*U*
1	Effect of seabed distance on bare UUV	(1.5, 2, 2.5, 3, 5, 7, 9, 10)	(0.5, 1, 2, 4)
2	Subsea distance effect on self-propelled UUV	(1.5, 2, 2.5, 3, 5, 7, 9, 10)	(0.5, 1, 2, 4)

3. Numerical Methods

To evaluate the hydrodynamic performance of the bare UUV and the self-propelled UUV, as well as the self-propulsion performance near subsea, the ANSYS FLUENT 17.0 was used to solve the governing equations. The Moving Reference Frame (MRF) model and $SST-kw$ turbulence model are used. The governing equations are discretized by the finite-volume method, where convective and diffusive terms in the equations are discretized with second-order-upwind differential format, central differential format, respectively. To speed up the convergence, the Couple method is used to solve the discrete equations.

3.1. Governing Equations

The Reynolds average equation includes: the continuum equation, and the momentum equation, as shown in Equations (12) and (13).

$$\frac{\partial \rho}{\partial t} + \frac{\partial \rho \overline{u}_i}{\partial t} = 0 \tag{12}$$

$$\frac{\partial}{\partial t}(\rho \overline{u}_i) + \frac{\partial}{\partial t}(\rho \overline{u}_i \overline{u}_j) = -\frac{\partial P}{\partial x_i} + \frac{\partial}{\partial x_j}\left[\mu\left(\frac{\partial \overline{u}_i}{\partial x_j} + \frac{\partial \overline{u}_j}{\partial x_i} - \frac{2}{3}\delta_{ij}\frac{\partial \overline{u}_l}{\partial x_l}\right)\right] - \frac{\partial}{\partial x_j}\left(\rho \overline{u_i' u_j'}\right) + F_i \tag{13}$$

u_i is the fluid velocity component. P is the total pressure. F_i is the volume force term. Additionally, μ is the dynamic viscosity coefficient. The $SST-kw$ turbulence model is used to simulate the turbulence terms in the *RANS* equations. This model is able to simulate turbulent shear stress transport and accurately predict the flow separation under the inverse pressure gradient. Turbulence kinetic energy and turbulence dissipation rate are calculated by the following equations.

$$\frac{\partial}{\partial t}(\rho k) + \frac{\partial}{\partial x_i}(\rho k u_i) = \frac{\partial}{\partial x_j}\left(\Gamma_k \frac{\partial k}{\partial x_j}\right) + G_k - Y_k + S_k \tag{14}$$

$$\frac{\partial}{\partial t}(\rho w) + \frac{\partial}{\partial x_i}(\rho w u_i) = \frac{\partial}{\partial x_j}\left(\Gamma_w \frac{\partial w}{\partial x_j}\right) + G_w - Y_w + D_w + S_w \tag{15}$$

To investigate the effect of *Hd* and Re_L on the hydrodynamic performance of the self-propelled UUV and the coupling effect of the hull and the propeller, firstly, it is necessary to obtain the rotational speed of the propeller under different operating conditions, and then solve the hydrodynamic performance and self-propulsion factor of the UUV. The rotational speed of propeller is corrected by the DEFINE_ZONE_MOTION macro once every 1000 iterations. The rotational speed for self-propelled point is considered to be obtained when the rotational speed value of the previous step does not change more than 0.01% with respect to the previous rotational speed correction value and the relative error

between the drag of the UUV and the thrust of the propeller does not exceed 0.01%. The propeller rotational speed is calculated according to the following equation.

$$N = N' + \frac{F_{uuv} + F_{balde}}{F_{uuv}} \delta_n \tag{16}$$

N' is the currently rotational speed. F_{uuv} is the drag of the UUV without propeller. F_{blade} is the thrust of the propeller. δ_n is the convergence coefficient.

3.2. Computational Domain and Boundary Conditions

The computational domain contains two parts: the stationary domain and the rotational domain. The cross section of the stationary domain is a square with a length and width of 20 D_A, which is the diameter of the maximum cross section of the UUV. The length of the flow field domain is 10 L_A, which is the length of UUV to ensure the full development of both the upstream incoming flow and wake flow, and the nose is 4 L_A from the inlet boundary. The rotating domain is a cylinder with a diameter of 200 mm and a length of 60 mm. The detailed sizes of the domain and the boundary condition settings are shown in Figure 2. Information about the flow field is transferred between the stationary and rotating domains through an interface. By reference to the findings of other researchers, the size of this flow field domain satisfies the requirements of the calculation. Additionally, the results of the validation cases that adopt the same strategy show that the size of the computational domain is reasonable.

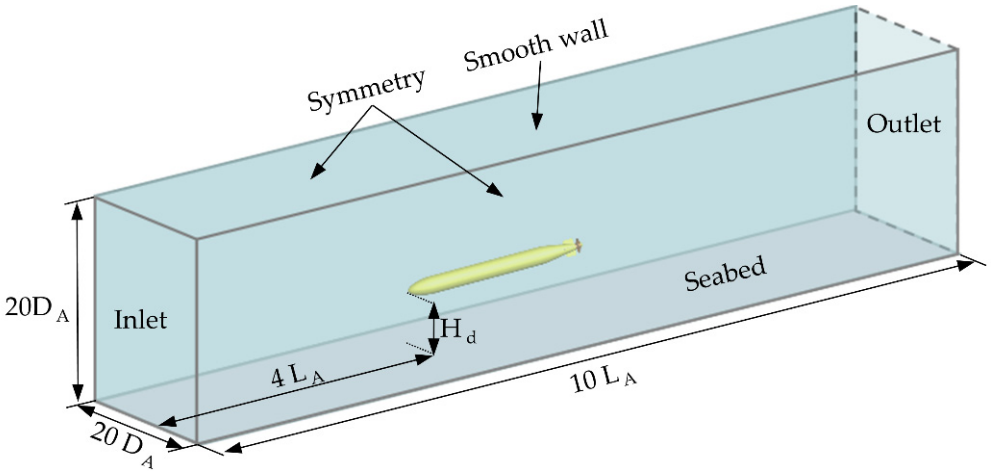

Figure 2. Schematic of flow field.

Inlet: Uniform incoming flow; $\vec{u} = \vec{u_c}$;
Outlet: Pressure outlet; $p = 0$;
Non-slip wall surfaces: For the hull, fin and propellers and subsea walls. $\vec{u} = 0$;
Slip wall surfaces: For the top of the flow field. $\frac{\partial \vec{u}}{\partial x_i} = 0$;
Symmetric boundary: For the side of the flow fields. $u_n = \vec{u_c} \cdot \vec{n} = 0$.

3.3. Meshing Settings

Ansys fluent mesh is applied to discrete the computational domain. The stationary domain is a mixed mesh containing polyhedral mesh and hexahedral mesh, and the rotating domain is a polyhedral mesh, as shown in Figure 3. In order to effectively and accurately predict the hydrodynamic properties of the UUV and propeller, two layers of encrypted regions are set up around the UUV and propeller, as shown in Figure 3a. Figure 3b shows the nose grid and Figure 3c shows the stern and rotation domain grid. To capture the shape of the propeller, the grid size of the leading and trailing edges of the propeller is 0.05 mm. Figure 3d shows the grid of the propeller blade surface. Prismatic boundary

layer meshes are set for all the non-slip boundaries in the flow field domain, and the height Y+ of the mesh is controlled to be around 1 to meet the needs of the turbulence model. A total of 15 boundary layers are set up. In order to capture the effects of the seabed on the hydrodynamics of the vehicle, the bottom wall of the stationary domain is arranged with 100 nodes in the length of $1L_A$.

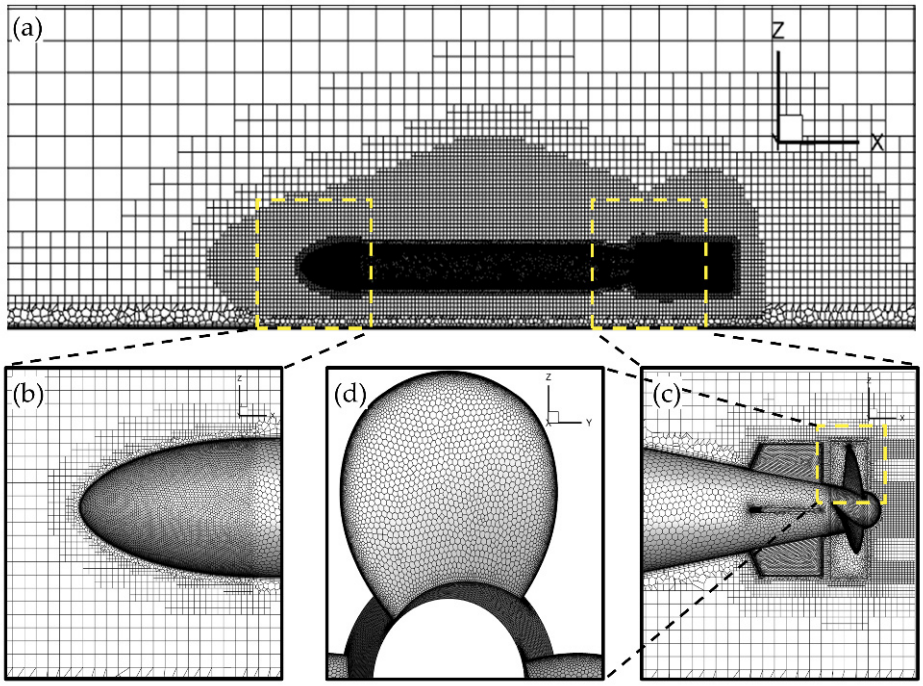

Figure 3. Grid settings. (**a**) The longitudinal profile grid of the domain with *HD* of 1.5; (**b**) UUV nose grid; (**c**) UUV tail grid; (**d**) propeller grid.

A grid independent validation is performed in this paper to confirm that the numerical results do not depend on the quantity of grids. Three grid resolutions, 3.2 M (coarse grid), 6 M (medium grid) and 8.4 M (fine grid), are set for the self-propelled UUV case with *Hd* of 2 and oncoming velocity of 1 m/s. Table 4 summarizes the numerical results for different grid resolutions. It can be seen that the numerical results of the fine and medium meshes are close to each other, which predicts that further increment of the number of mesh will not significantly affects the numerical results of CFD. Therefore, the medium resolution grid is used to complete the subsequent numerical simulations. In order to eliminate the influence of grid resolution on the numerical results of different simulation cases, the medium grid resolution is used for the bare UUV simulation cases and the self-propelled UUV cases.

Table 4. Grid-independence verification.

Grid Cell (M)	C_l	m_y	K_T	K_Q
3.2	0.0255	0.0089	0.1087	0.0248
6	0.0248	0.0085	0.1070	0.0234
8.4	0.0246	0.0084	0.1061	0.0236

3.4. Verification of Numerical Method

Due to the lack of experimental data for the self-propelled model, the articles adopt the same validation strategy as the others [1–4]. Numerical simulations of the UUV and propeller from the available experimental study data are carried out separately to verify the feasibility of the numerical method used in the paper.

The SUBOFF is an axisymmetric vehicle and the hydrodynamic test is carried out by David Taylor Research Center. It is aimed at providing a data base for CFD validation

and other flow field analysis related to submarines. A large number of academics adopt SUBOFF as a research object for UUV. The AFF-3 model in SUBOFF is chosen in this paper to verify the feasibility of the numerical method. Huang et al. [16] experimentally studied the hydrodynamic performance of the AFF-8 model at a Re_L of 12×10^6. The wake characteristics of the AFF-2 model at Re_L 1.1×10^6 were investigated by Jiménez et al. [17] through wind tunnel tests. Posa et al. [18] investigated the turbulent boundary layer on the surface of the AFF-8 model with a Re of 1.2×10^6 by CFD method.

The distribution of pressure coefficient (C_p) with Re_L of 1.2×10^6 is obtained by CFD method. C_p is calculated by Equation (17). The comparison of the numerical results is given in Figure 4. It can be seen that the distribution of C_p on the hull surface agrees well with the results of other researchers, except that field near the fin plate of the model. The main reason for the phenomenon is the absence of a bridge in the AFF-3 model. The differences in the geometric models lead to the divergence in the flow field distribution at the leading edge of the stern appendages.

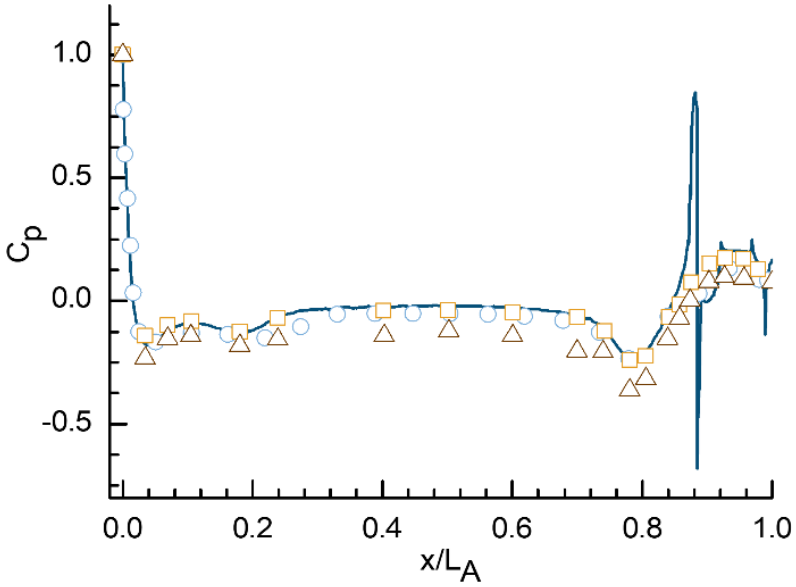

Figure 4. Pressure coefficient of SUBOFF AFF−3. Present result: — Plane *a* on the side of the negative *z* axis; ○ Posa et al. at Re_L 1.2×10^5; □ Huang et al. (1994) at $Re_L = 12 \times 10^6$; △ Jiménez et al. (2010a) at $Re_L = 1.1 \times 10^6$.

There are two reasons for the discrepancy.

1. The geometric profile of the model used in the article is different from that of [16–18]. The geometric model in the article contains the stern appendages, but not the fair-water, while [16,18] contain both the stern appendages and the fair-water, and [17] has neither the stern appendages nor the fair-water.
2. The most significant reason is that the cross section of [16–18] from which the C_p is obtained did not pass through the stern appendages, while the cross section of this paper passed through it.

The DTMB 4119 propeller has been used to verify the reliability of numerical methods and has been widely applied to research the cavitation performance of the propeller. The open water characteristics of this propeller were obtained by CFD method and compared with the experimental results. As shown in Figure 5, the numerical results agree well with the experimental results. The largest discrepancy appears in the efficiency variable with J of 0.833, with a relative error of 2.57%, which can be accepted. The experimental results for this propeller were obtained from reference [19].

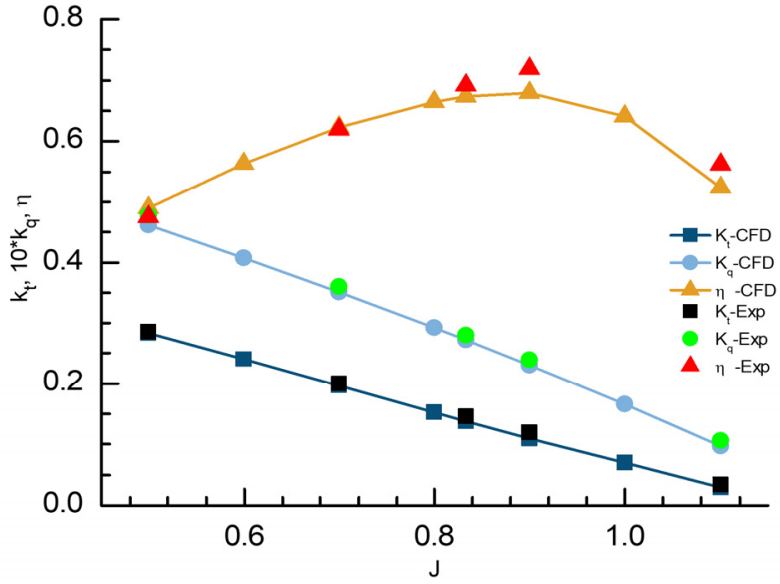

Figure 5. Verification of open water performance of DTMB4119.

4. Results and Discussion

4.1. The Hydrodynamic Characteristics of Near-Seabed Bare UUV

The hydrodynamic characteristics of the bare UUV near the seabed includes drag, lift and pitching moment characteristics. The variation of the hydrodynamic characteristics of the bare UUV near the seabed with *Hd* and Re_L are given in Figures 6–8. Figure 9 shows the C_p distribution of UUV cross-section (a) for each *Hd* case when the speed is 0.5 m/s. Cross-section (a) is defined by Figure 1, which is the longitudinal section of the UUV. Figure 10 shows the C_p distribution of UUV at cross-section (a) for *Hd* of 1.5 and Re_L of 1×10^6~8×10^6. The C_p is defined by Equation (17), where P_0 is the statics pressure value at the inlet and V_0 is the fluid velocity at the inlet.

$$C_p = \frac{P - P_0}{\frac{1}{2}\rho V_0^2} \tag{17}$$

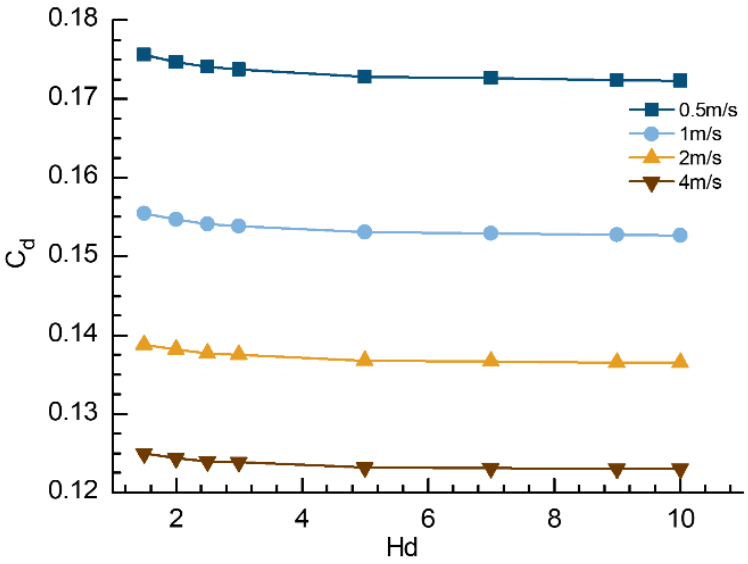

Figure 6. Bare UUV resistance characteristics.

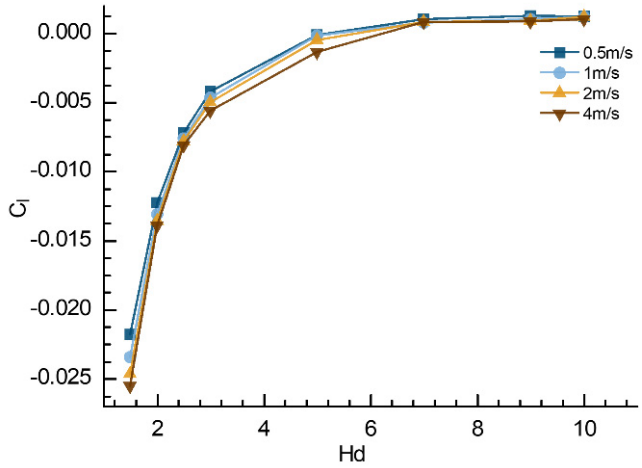

Figure 7. Bare UUV lift characteristic.

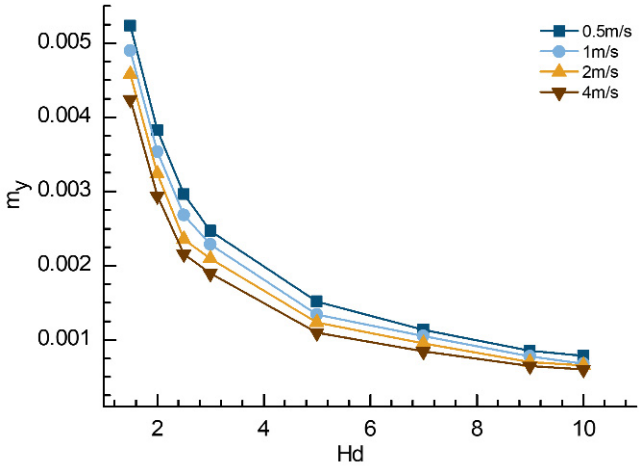

Figure 8. Bare UUV Pitch moment characteristics.

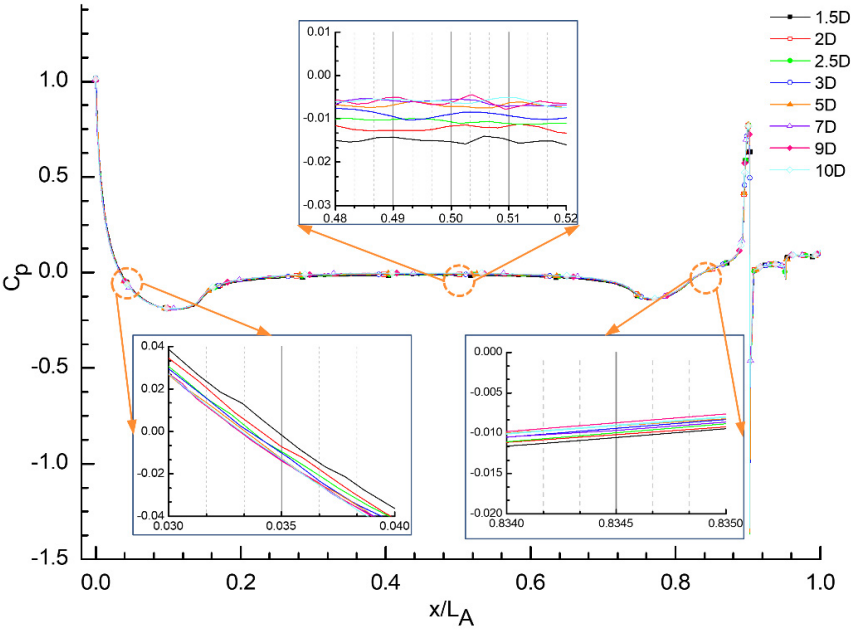

Figure 9. C_p distribution of bare UUV at cross section a for different *Hd*.

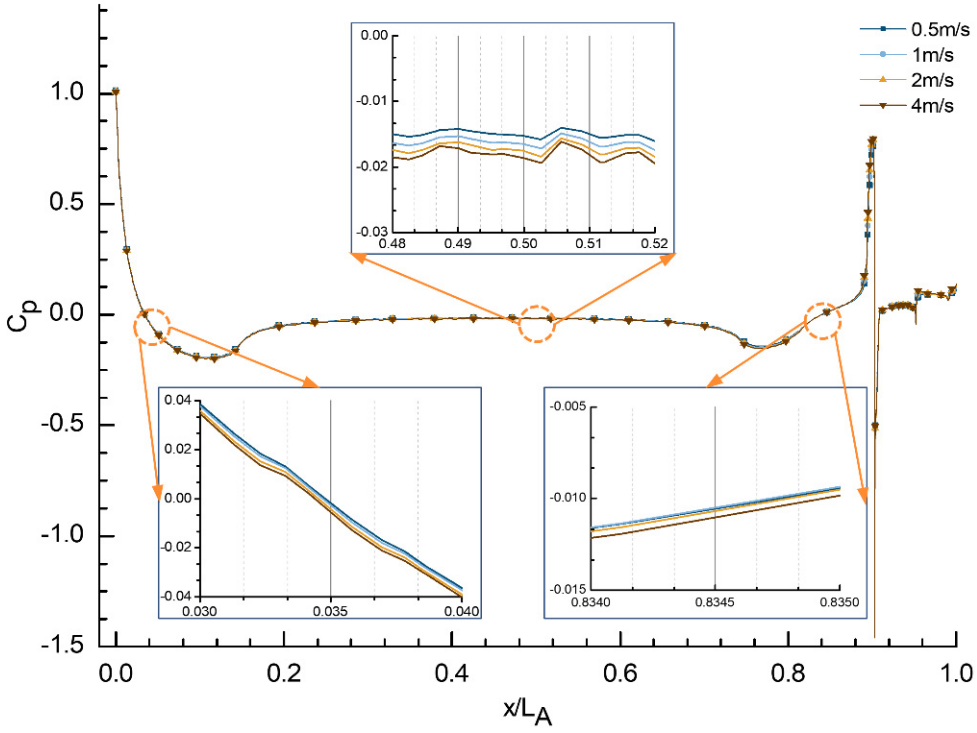

Figure 10. C_p distribution of bare UUV at cross section a for different Re_L.

4.1.1. Correlations between Hydrodynamic Characteristics of Bare UUV and *Hd*

- Drag Characteristics

The drag coefficient of the bare UUV decreases continuously with the increase of *Hd* and finally tends to be stable, and the variation rate of the coefficient is the largest near the seabed. As shown in Figure 6, the drag coefficient of UUV is greater near the seabed. When *Hd* is greater than 5, the drag coefficient tends to be stable and remains constant. This blocking effect between the UUV and the seabed causes an increase in the differential pressure in the X-direction on the UUV surface. Figure 9 shows that the C_p value is greater than 0 until 3.5% L_A, and decreases with increasing *Hd*. When *Hd* is greater than 5, the C_p is almost constant. The value C_p near the nose of the UUV decreases continuously with the increase of *Hd*, that is, the pressure near the nose along the X-direction decreases with the increase of *Hd*. The pressure component in the X-direction of the parallel section of the UUV is 0, so it is ignored. The C_p value near 83.45% L_A is less than 0, and the absolute value of C_p decreases continuously with the increase of *Hd*. That is, the pressure value there increases continuously with the increase of *Hd* increases.

The drags of the bare UUV are mainly contributed from the sum of the pressure values of the nose and tail. The variation of the tail pressure value is one order of magnitude smaller than that of the nose pressure. When *Hd* is greater than 5, both are of the same order of magnitude. When *Hd* is less than 5, the drag of the UUV is mainly determined by the component of the pressure at the nose of the UUV along the X-direction. As *Hd* increases, the drag of UUV decreases. When *Hd* is greater than 5, the drag of UUV is almost constant.

- Lifting Characteristics

Absolute value of lift coefficient of bare UUV decreases continuously with the increase of *Hd* and finally tends to be zero, and the variation rate of the coefficient is the greatest near the seabed. As shown in Figure 7, the absolute value of lift coefficient of UUV near seabed is larger than that away from seabed, which is shown as the ground diving phenomenon near seabed without angle of attack. This phenomenon benefits from the asymmetric distribution of pressure on the upper and lower surfaces of the UUV, as shown in Figure 15. A further reason is due to the blocking effect between the UUV and the seabed. This

leads to an increase in the fluid velocity between them and consequently a decrease in the static pressure value at that position, which eventually leads to a lift of the UUV less than 0. Figure 9 shows that the pressure at the nose and parallel segments varies with *Hd*. When X/L_A is greater than 3.5%, the surface pressure coefficient of the UUV is less than 0. Additionally, the absolute value of the pressure coefficient decreases continuously with the increase of *Hd*. The absolute value of the parallel segment C_p decreases continuously with the increase of *Hd*. When *Hd* is greater than 7, the absolute value of parallel segment C_p is almost unaffected by the seabed. Therefore, the absolute value of UUV lift keeps decreasing with the increase of *Hd*, and when *Hd* is greater than 7, the UUV lift is almost constant.

- Pitch Moment Characteristics

The center of buoyancy of the bare UUV is treated as the origin of the pitching moment. The pitching moment coefficient of the bare UUV decreases with the increase of *Hd* and finally tends to be zeros. Additionally, the variation rate of the coefficient is the greatest near the seabed. As shown in Figure 8, the pitching moment coefficient of UUV near seabed is greater than that away from seabed. There is a tendency of the UUV to dive in the near-seabed case. The lift coefficients on the UUV surface are unevenly distributed along the X-direction. It can be seen from Figure 9 that the lift coefficient before the buoyancy center is larger than that after the buoyancy center. The rule of variation of the bare UUV pitching moment with *Hd* is consistent with that of the lift coefficient.

4.1.2. Correlation between the Hydrodynamic Characteristics of Bare UUV and Re_L

From Figures 6–8, some remarks can be concluded. The UUV drag coefficient decreases with the increase of Re_L. The absolute of lift coefficient increases with the increase of Re_L. When *Hd* is greater than 7, the relationship between lift coefficient and pitching moment coefficient and Re_L becomes weaker.

From Figure 10, it can be found that the C_p near the nose of the UUV decreases with increasing Re_L, while the absolute value of C_p near the tail increases with increasing Re_L. As a result, the differential pressure drag of the UUV decreases with increasing Re_L, while the frictional drag coefficient remains constant in this Re_L range. Finally, the drag coefficient of the UUV decreases with increasing Re_L. The C_p values of UUV are less than 0 behind 3.5% L_A, and the C_p values decrease with increasing Re_L. This explains that the absolute values of UUV lift and pitching moment increase with increasing Re_L.

The variation rule of pitch moment coefficient with Re_L is not consistent with the lift coefficient because the increment of pitch moment with velocity is smaller than the second-squares increment of velocity.

4.2. Hydrodynamic Characteristics of Self-Propelled UUV near the Seabed and the Self-Propelled Performences

4.2.1. Hydrodynamic Characteristics of the Self-Propelled UUV in Relation to the *Hd* and Re_L

The drag coefficient of the self-propelled UUV decreases continuously with the increase of *Hd* and finally tends to be stable, and the variation rate of the coefficient is the largest near the seabed. Figure 11 shows that the drag coefficient of self-propelled UUV near the seabed is greater than that away from seabed. When *Hd* is greater than 5, the drag coefficient tends to be stable and remains constant. The drag coefficient of the self-propelled UUV increased by 16.74~17.88% compared to that of the bare UUV.

The absolute value of the lift coefficient of the self-propelled UUV decreases continuously with the increase of *Hd* and finally tends to be around 0.008, and the variation rate of the coefficient is the largest near the seabed. As can be seen from Figure 12, the absolute value of the lift coefficient of self-propelled UUV near the seabed is greater than that away from seabed. When *Hd* is greater than 7, the lift coefficient of UUV tends to be constant. It is consistent with the trend of the lift coefficient of bare UUV with *Hd*. However, the lift coefficient of the self-propelled UUV increases by 69~130% compared to that of the bare UUV when the *Hd* less than 3.

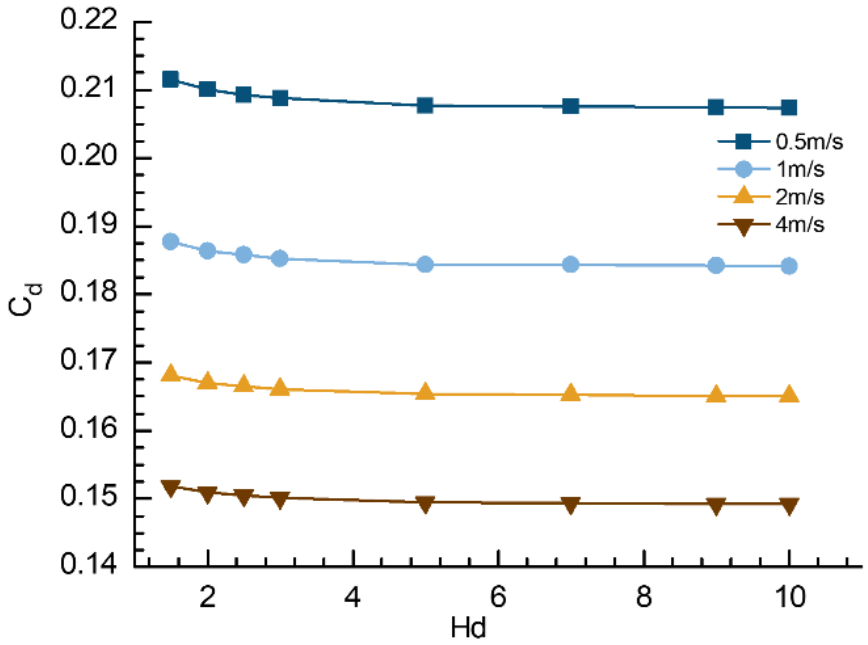

Figure 11. Self-propelled UUV drag characteristics.

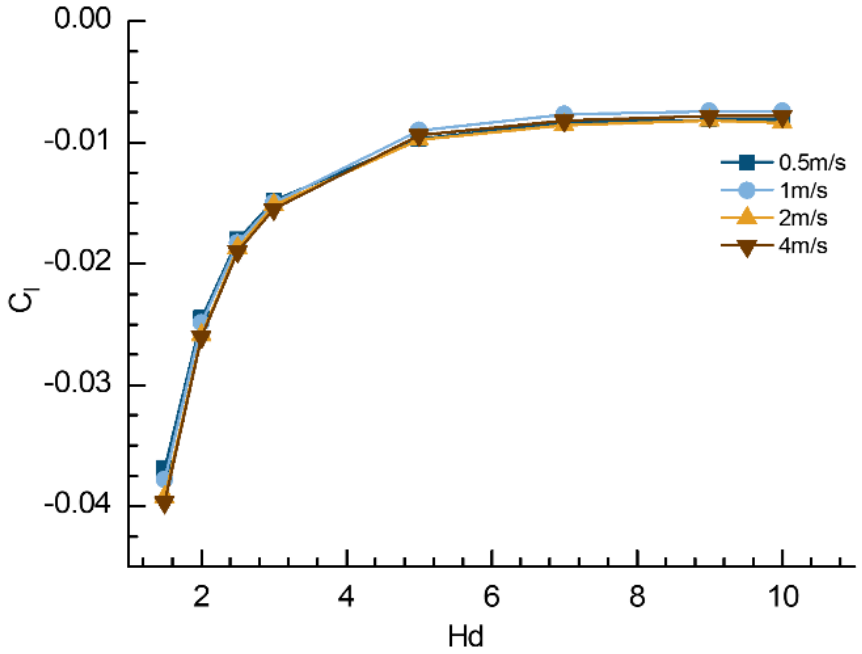

Figure 12. Self−propelled UUV lift characteristics.

Similar to the bare UUV, the self-propelled UUV takes the buoyancy center of the UUV with a propeller as the origin of the pitching moment. The pitch moment coefficient of the self-propelled UUV decreases with the increase of *Hd* and finally tends to be around 0.005, and the variation rate of the coefficient is the largest near the seabed. As can be seen from Figure 13, the pitching moment coefficient near the seabed is larger than that away from the seabed, which causes the dive phenomenon near the seabed without angle of attack. The pitching moment curve of the self-propelled UUV varies with *Hd* and Re_L according to the same trend as that of the bare UUV. However, the pitching moment coefficient of the self-propelled UUV increased by 100~300% relative to that of the bare UUV when the *Hd* less than 3.

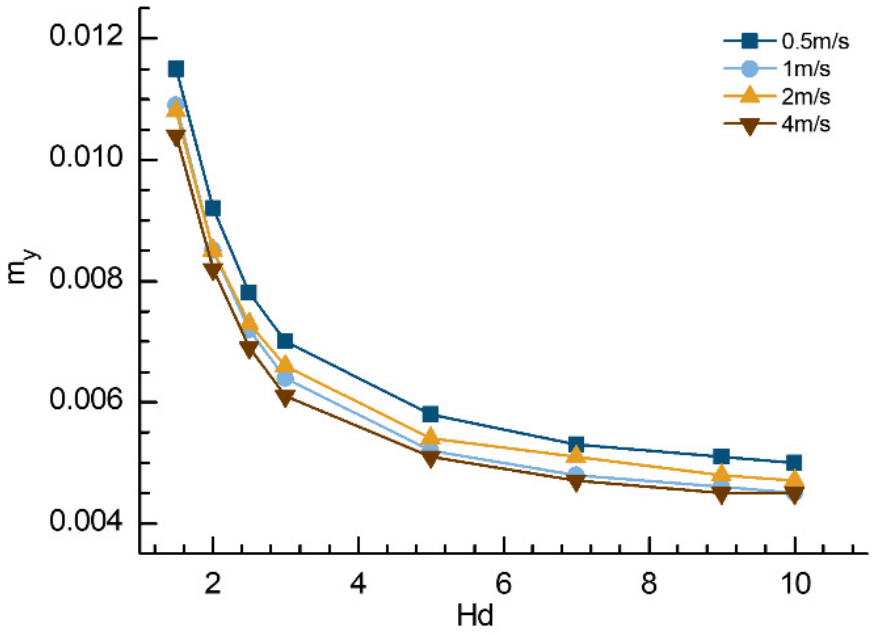

Figure 13. Self-propelled UUV Pitch moment characteristics.

The correlation of hydrodynamics coefficients of the self-propelled UUV and Re_L is consistent with that of the bare UUV. The drag coefficient decreases with the increase of Re_L. The absolute of lift coefficient increases with the increase of Re_L. The variation rule of pitch moment coefficient with Re_L is not consistent with the lift coefficient because the increment of pitch moment with velocity is smaller than the second-squares increment of velocity. When *Hd* is greater than 7, the relationship between lift coefficient and pitching moment coefficient and Re_L become weaker.

4.2.2. Effects of *Hd* and Re_L on UUV Self-Propelled Performance

The relevant self-propulsion coefficients are derived from Equations (8)–(11). To analyze the effects of *Hd* and Re_L on the interactions between the UUV and the thruster, parameters such as thrust reduction, hull efficiency, effective wake fraction, and rotational efficiency are selected for analysis. The first two of these parameters are the effects of the thruster on the UUV, and the last two reflect the effect of the UUV on the thruster.

- The Variation of Thrust Reduction

t describes the effect of propeller at the wake of the hull on the UUV. Due to the rotation of the thruster at the tail of the UUV, velocity of flow near the tail increases and the static pressure here decreases relative to the static pressure of the bare UUV, resulting in an increase in the drag of the UUV. For the increased UUV drag, its convention is generally attributed to the reduced thrust of the propellor.

As can be seen from Figure 14, *t* decreases firstly with the increasing of *Hd*, then increases slowly and finally tends to stable. Near the seabed, the wall blocking effect of the seabed increases the pressure difference between the lead and tail of the UUV. Additionally, there is an abrupt change in the *t* curve for *Hd* equal to 2.5. This is because that although the trends of R_0, *R* and *T* with *Hd* are consistent, the inconsistency of the rapidity of their changes leads to an abrupt change in *t* when *Hd* is 2.5. In addition, comparing the *t* values for different *Hd*, it is found that the relative change of *t* with respect to that at *Hd* of 10 is less than 1%. It suggests that the effect of the seabed wall on *t* is relatively weak. It is difficult to capture the small changes by numerical methods. *t* increases with the increase of Re_L.

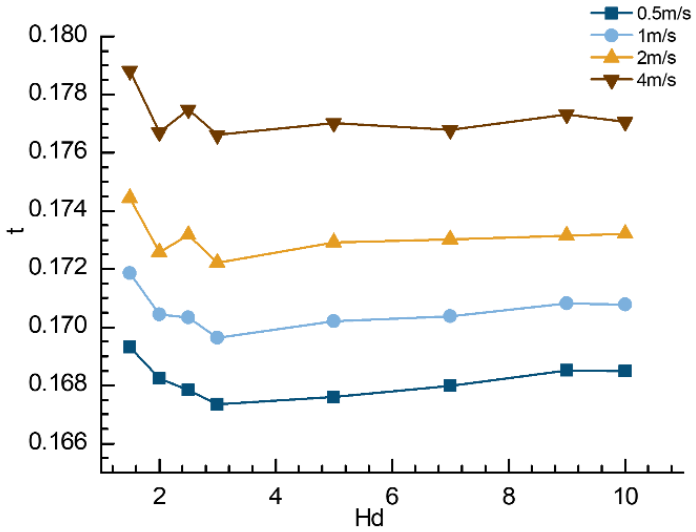

Figure 14. Thrust reduction for self-propelled UUV.

Figure 15 shows the pressure distribution of self-propelled UUV at cross-section (a) with Hd = 1.5 and oncoming flow velocities of 0.5, 1, 2, 4 m/s, where (a) is the pressure distribution of bare UUV and (b) is the pressure distribution of UUV with propeller. Comparing the two columns (a) and (b), it can be seen that the pressure at the tail end of the UUV decreases due to the suction effect of the propeller, which in turn causes an increase in the drag of the vehicle, corresponding to a reduction in the thrust of the UUV.

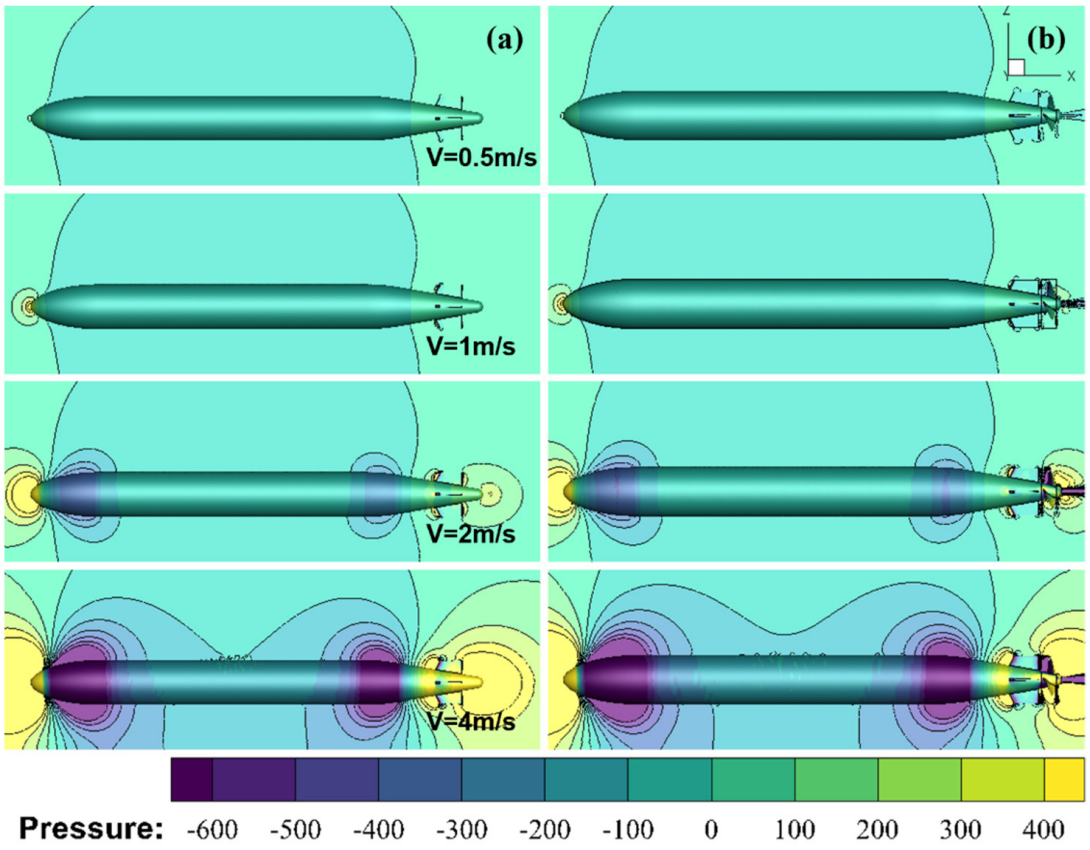

Figure 15. The pressure clouds at the bare UUV as shown columns (**a**) and self−propelled UUV as shown columns (**b**) at cross−section a.

Figure 16 shows the pressure distribution of UUV at a cross section with incoming flow velocity of 0.5 m/s and *Hd* of 1.5, 2, 2.5, 3, 5, 7, 9, 10, where (a) column is the pressure distribution of bare UUV and (b) column is the pressure distribution of UUV together with propeller. Comparing the two columns (a) and (b), it can be seen that the pressure at the trailing end of the UUV is reduced due to the suction of the propeller, which in turn causes an increase in the drag of the UUV.

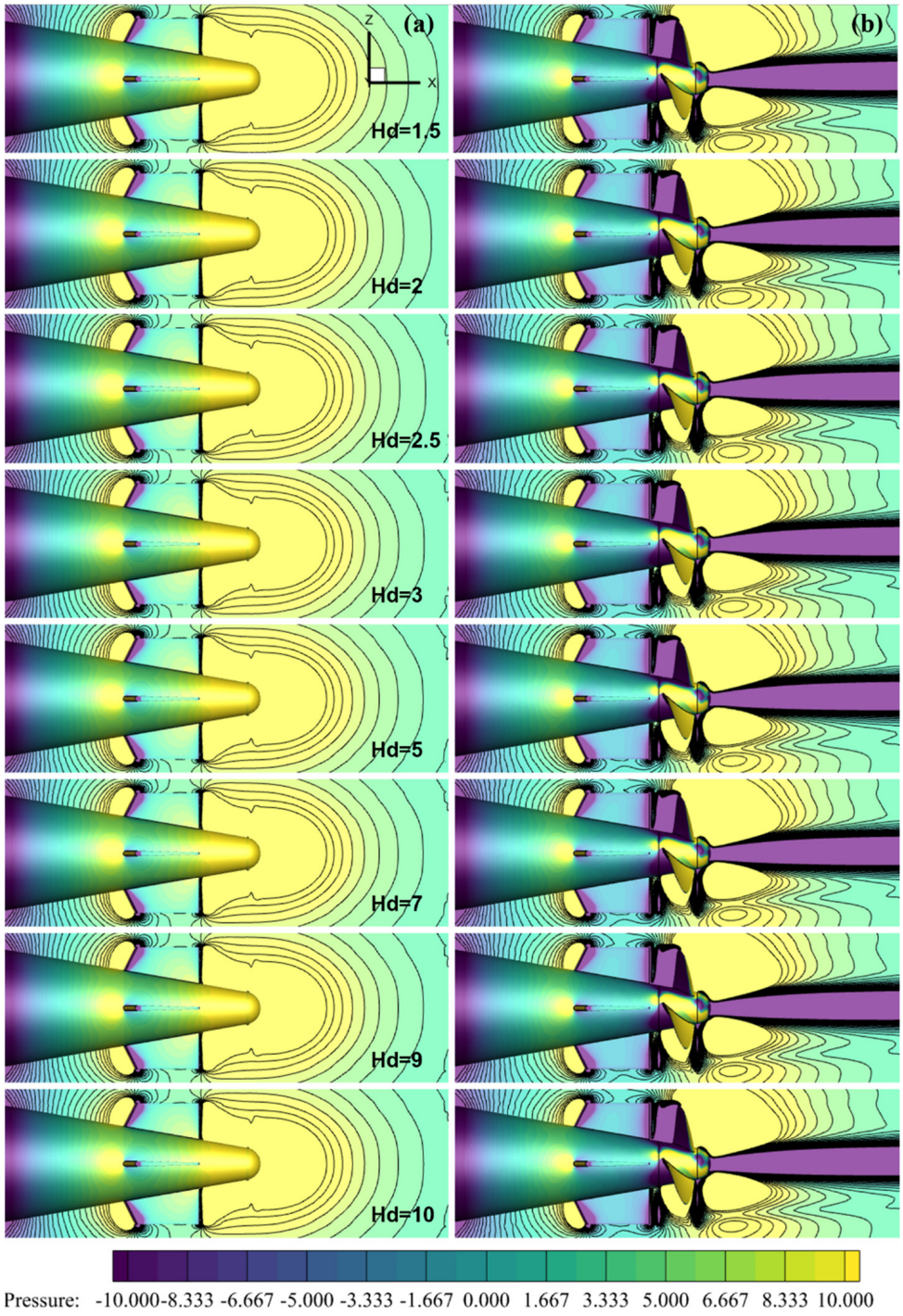

Figure 16. The pressure clouds at the bare UUV as shown columns (**a**) and self-propelled UUV as shown columns (**b**) at a cross-section.

- Hull Efficiency

η_H depicts the hull efficiency and represents the combined effect of thrust reduction and wake flow. As can be seen from Figure 17, this efficiency decreases with increasing Re_L. As Hd increases, this efficiency gradually increases and remains stable when Hd is greater than 3.

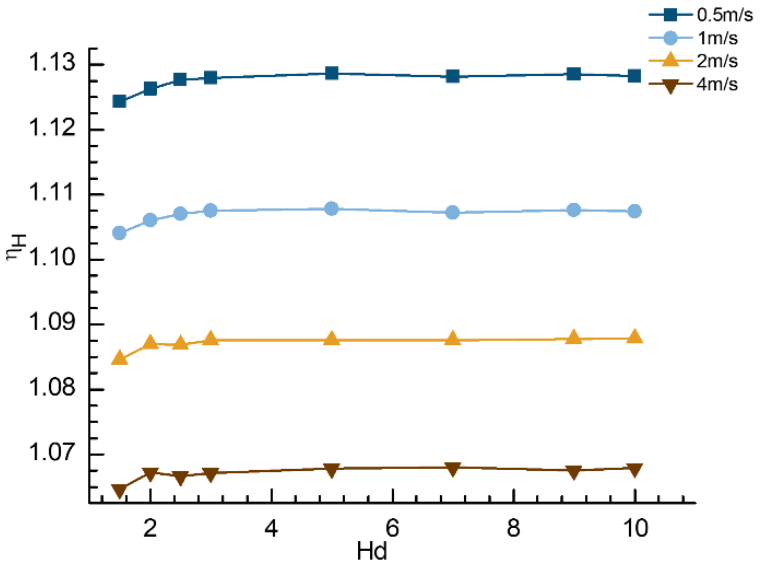

Figure 17. Hull efficiency for self-propelled UUV.

- Effective Wake Fraction of Self-Propelled UUV

As shown in Figure 18, w increases slowly with the increasing of Hd and finally stabilizes, and w decreases with the increase of Re_L. Figure 19 shows the distribution of the w at the UUV propeller disc with Hd of 1.5 and oncoming velocities from top to bottom of 0.5 m/s, 1 m/s, 2 m/s, and 4 m/s. (a) is the nominal wake at the bare UUV propeller disc, and (b) is the effective wake at the propeller disc. The w in the cloud plot is calculated from Equation (18). V_A is the speed at the propeller disc. Additionally, V represents the UUV's speed.

$$w = 1 - \frac{V_a}{V} \tag{18}$$

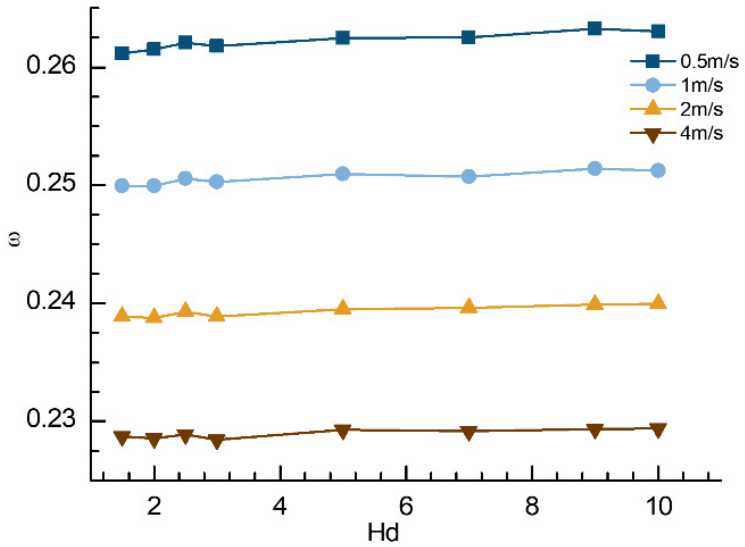

Figure 18. Effective wake current fraction of self-propelled UUV.

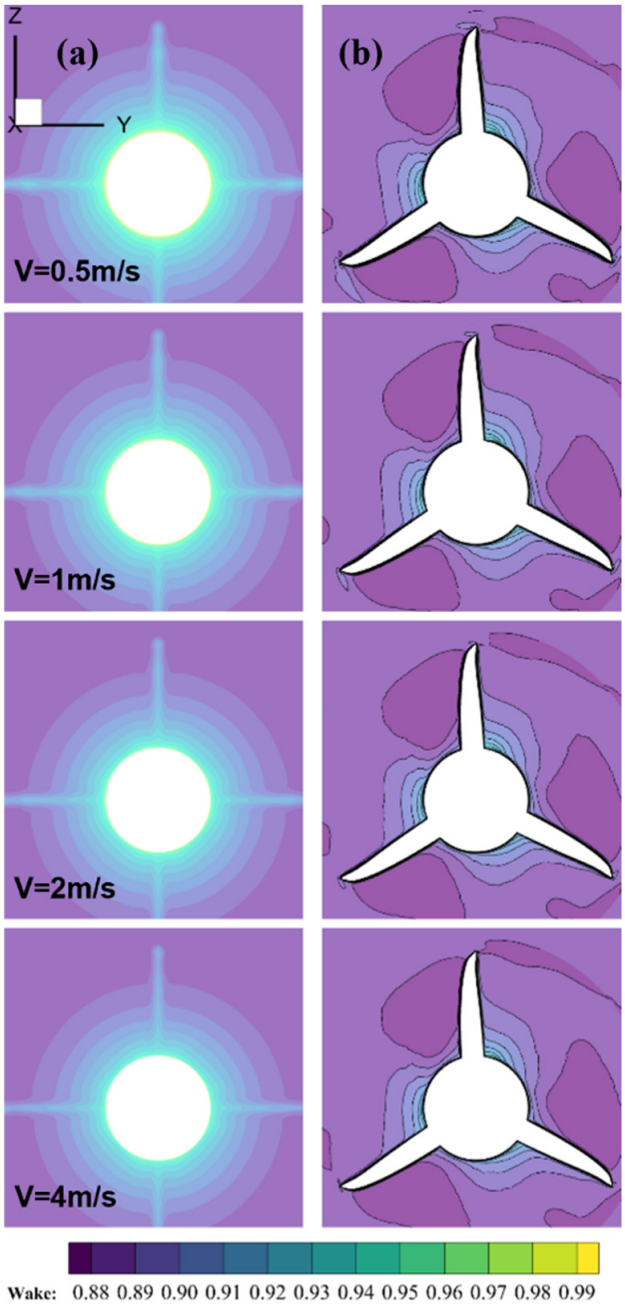

Figure 19. Cloud diagram of the wake fraction at the propeller disc for various Re_L when Hd is 1.5. Columns (**a**) are for the bare UUV, and columns (**b**) are for the self-propelled UUV.

Figure 19 shows that the effective wake is smaller than the nominal wake, and the effective wake decreases with increasing Re_L, which is consistent with Figure 18. The shear layer formed at the trailing edge of the UUV fin plate and the turbulent boundary layer grows along the tail of the UUV together form the cross-shaped wake field at the propeller disc in Figure 19a.

Figure 20 shows the distribution of the wake fraction w at the propeller disc of UUV with 8 kinds of different Hd at the oncoming velocity of 0.5 m/s, (a) the nominal wake at the propeller disc of bare UUV and (b) the effective wake at the propeller disc of self-propelled UUV. Figure 20 shows that the effective wake flow is smaller than the nominal wake flow, and the effective wake flow is weak with the variation of Hd, which can hardly be seen in the cloud diagram.

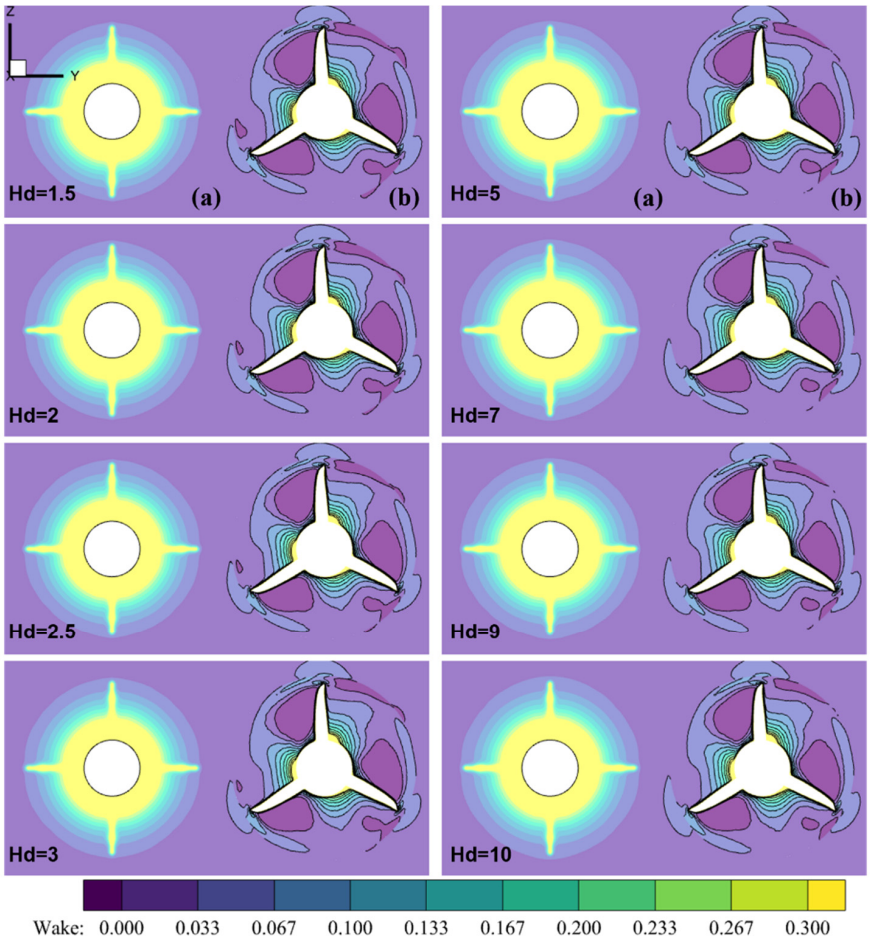

Figure 20. Cloud diagram of the wake fraction at the propeller disc for various *Hd* for oncoming velocity of 0.5 m/s. Columns (**a**) are for the bare UUV, and columns (**b**) are for the self-propelled UUV.

- Efficiency of Propeller Rotation

The efficiency η_i increases with the increase of *Hd* at low Re_L and it is almost independent of *Hd* when *Hd* is greater than 7. It increases with the increase of Re_L. At large Re_L, the efficiency is weakly correlated with *Hd*, as shown in Figure 21.

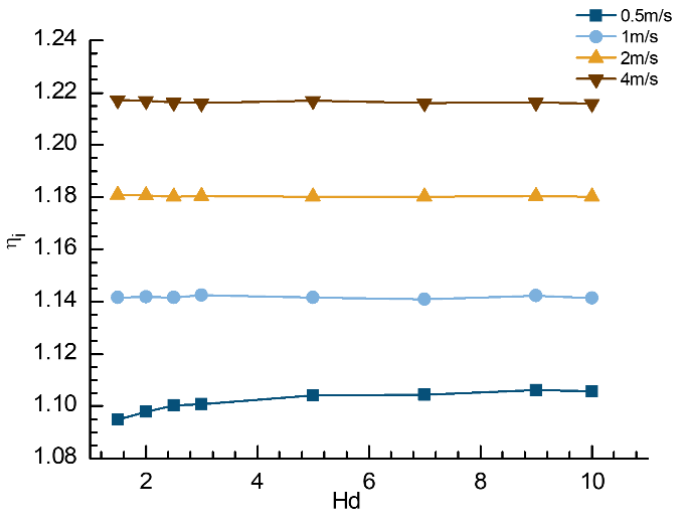

Figure 21. Efficiency of propeller rotation.

5. Conclusions

The variation trend of hydrodynamic performance of bare UUV and self-propelled UUV with Hd and Re_L is similar. The coefficient of drag decreases with the increase of Hd and finally tends to be stable. The absolute value of lift coefficient decreases with the increase of Hd and finally tends to be zeros. The coefficient of pitching moment decreases with the increase of Hd and finally tends to be zeros. The hydrodynamic coefficients of UUV have a significant rate of variation near the seabed. The drag coefficient decreases with increasing Re_L. The absolute value of the lift coefficient increases with increasing Re_L. The pitching moment coefficient changes in the opposite trend of the lift coefficient. The drag coefficient of the self-propelled UUV increases by 16.74~17.88%. Additionally, lift coefficient, pitching moment coefficient of the self-propelled UUV increase by 69~130% and 100~300%, respectively, compared with that of bare UUV when UUV near the seabed. Thrust reduction, hull efficiency, wake fraction and rotational efficiency are weakly correlated with Hd. It is found that the thrust reduction and rotational efficiency increase with increasing Re_L, and the hull efficiency and associated flow fraction decrease with increasing Re_L.

The case of UUV for straight sailing were discussed for the paper. In the future, it is necessary to study the effect of seabed on the hydrodynamic performance of the self-propelled UUV with variations of the angle of attack.

Author Contributions: Conceptualization, Z.M., Y.H. and W.T.; validation, X.L.; formal analysis, W.T. and X.L.; data curation, X.L.; writing—original draft preparation, X.L.; writing—review and editing, W.T.; funding acquisition, Z.M. and W.T. All authors have read and agreed to the published version of the manuscript.

Funding: This research was funded by the National Natural Science Foundation of China (Program No. 51809214) and the Fundamental Research Funds for the Central Universities for Wenlong Tian.

Institutional Review Board Statement: Not applicable.

Informed Consent Statement: Not applicable.

Conflicts of Interest: The authors declare no conflict of interest.

References

1. Sezen, S.; Dogrul, A.; Delen, C.; Bal, S. Investigation of Self-Propulsion of DARPA Suboff by RANS Method. *Ocean Engineering* **2018**, *150*, 258–271. [CrossRef]
2. Dogrul, A.; Sezen, S.; Delen, C.; Bal, S. Self-Propulsion Simulation of DARPA Suboff. 9. In *Developments in Maritime Transportation and Harvesting of Sea Resources*; CRC Press: Boca Raton, FA, USA, 2017.
3. Posa, A.; Balaras, E. Large-Eddy Simulations of a Notional Submarine in Towed and Self-Propelled Configurations. *Comput. Fluids* **2018**, *165*, 116–126. [CrossRef]
4. Chase, N.; Carrica, P.M. Submarine Propeller Computations and Application to Self-Propulsion of DARPA Suboff. *Ocean. Eng.* **2013**, *60*, 68–80. [CrossRef]
5. Vali, A.; Saranjam, B.; Kamali, R. Experimental and Numerical Study of a Submarine and Propeller Behaviors in Submergence and Surface Conditions. *JAFM* **2018**, *11*, 1297–1308. [CrossRef]
6. Tian, W.; Song, B.; Ding, H. Numerical Research on the Influence of Surface Waves on the Hydrodynamic Performance of an AUV. *Ocean. Eng.* **2019**, *183*, 40–56. [CrossRef]
7. Wang, L.; Martin, J.E.; Felli, M.; Carrica, P.M. Experiments and CFD for the Propeller Wake of a Generic Submarine Operating near the Surface. *Ocean. Eng.* **2020**, *206*, 107304. [CrossRef]
8. Zhang, N.; Zhang, S. Numerical Simulation of Hull/Propeller Interaction of Submarine in Submergence and near Surface Conditions. *J. Hydrodyn.* **2014**, *26*, 50–56. [CrossRef]
9. Song, B.W.; Zhu, X.Y.; Cao, Y.H.; Liang, Q.W. Strategy and Key Technologies of UUV Parking on the Seabed. *Torpedo Technol.* **2010**, *18*, 401–405.
10. Zhu, X.Y.; Song, B.; Xu, G.; Yang, S. Research on Landing Strategy and Influencing Factors of an Autonomous Underwater Vehicle with Supporting Mechanism. *J. Shanghai Jiaotong Univ.* **2017**, *51*, 1241. [CrossRef]
11. Zhu, X.Y.; Song, B.; Wang, P. Hydrodynamic Characteristics Analysis of UUV Parking on the Seabed. *J. Shanghai Jiaotong Univ.* **2012**, *46*, 573.
12. Zhang, B.; Song, B.; MAO, Z.; Jiang, J. Stability Simulation for Underwater Glider Parking on Seabed. *J. Xi'an Jiaotong Univ.* **2016**, *50*, 49–55.

13. Aijun, Z.; Liangmei, Y.; Hong, Z. Resistance Test Method on Underwater Vessel Operating Close to the Bottom or the Surface. *J. Ship Mech.* **2012**, *16*, 368–374.
14. Du, X.; Wang, H.; Hao, C.; Li, X. Analysis of Hydrodynamic Characteristics of Unmanned Underwater Vehicle Moving Close to the Sea Bottom. *Def. Technol.* **2014**, *10*, 76–81. [CrossRef]
15. Yan, T.; Ma, D.; Xue, X.; Chen, X. Analysis of Hydrodynamic Characteristics of Autonomous Underwater Vehicle Close to Sea Bottom. *Comput. Simul.* **2016**, *33*, 301–305+327.
16. Huang, T.; Liu, H.L. *Measurements of Flows over an Axisymmetric Body with Various Appendages in a Wind Tunnel: The DARPA SUBOFF Experimental Program*; National Academy of Sciences, Engineering, and Medicine: Washington, DC, USA, 1994.
17. Jiménez, J.M.; Hultmark, M.; Smits, A.J. The Intermediate Wake of a Body of Revolution at High Reynolds Numbers. *J. Fluid Mech.* **2010**, *659*, 516–539. [CrossRef]
18. Posa, A.; Balaras, E. A Numerical Investigation of the Wake of an Axisymmetric Body with Appendages. *J. Fluid Mech.* **2016**, *792*, 470–498. [CrossRef]
19. Jessup, S.D.; Boswell, R.J.; Nelka, J.J. *Experimental Unsteady and Time Average Loads on the Blades of the Cp Propeller on a Model of the DD-963 Class Destroyer for Simulated Modes of Operation*; David W Taylor NAVAL Ship Research and Development Center Bethesda: Rockville, MD, USA, 1977.